

Modelling stars with Gaussian Process Regression – I: Augmenting Stellar Model Grid

Tanda Li,¹[★] Guy R. Davies,¹[†] Alex Lyttle,¹ Lindsey Carboneau,¹ and A. N. Others¹

¹ School of Physics and Astronomy, University of Birmingham, Birmingham, B15 2TT, United Kingdom

Accepted XXX. Received YYY; in original form ZZZ

ABSTRACT

Grid-based modelling is widely used for estimating stellar parameters. However, stellar model grid is sparse because of the computational cost. This paper demonstrates an application of the Gaussian Process (GP) Regression that turns a sparse model grid onto a continuous function. We train GP models to map five fundamental inputs (mass, equivalent evolutionary phase, initial metallicity, initial helium fraction, and the mixing-length parameter) to observable outputs (effective temperature, surface gravity, radius, surface metallicity, and stellar age). To overcome the limitation of training data size in the GP framework, we break up the model grid by the evolutionary stage, train each sub-section separately, and lastly combine multiple GP models. We test the GP predictions for the five outputs using off-grid stellar models and find no obvious systematic offsets, indicating good accuracy in predictions. However, we notice that the systematic uncertainties are not uniform across the parameter space because learned models are less precise around the hook and turn-off points where global parameters quickly vary. We solve this by training another GP model to describe systematic uncertainties. As a further validation, we apply these GP models to characterise 100 fake stars. Inferred masses and ages determined with GP models well recover true values within one standard deviation. We also notice that GP-based stellar ages are more precise than those estimated with the original grid because of the fully sampling of fundamental inputs.

Key words: Star: Modelling – Machine Learning – Gaussian Process

1 INTRODUCTION

Theoretical stellar model has been developed for decades to simulate star structure and evolution. Star modelling is mostly grid-based (e.g. Choi et al. 2016) because computing many stellar models are time-consuming especially when a number of free input parameters are considered. Varying one of these adjusted parameters (mass, metallicity, helium fraction, mixing-length parameter, etc.) adds on an input demission and hence exponentially increases the computational cost.

A sparse grid is not ideal for the statistics analysis. Classical method like interpolation has been applied to overcome this disadvantage. For instance, Dotter (2016) developed a method to transform stellar evolution tracks onto a uniform basis and then interpolate to construct stellar isochrones. More recently, Rendle et al. (2019) uses Bayesian statistics and a Markov Chain Monte Carlo approach to find a representative set of interpolated models from a grid. The interpolation of both works achieve good accuracy for 3-demission grids (inputs are mass, age, and metallicity). However, this approach becomes less reliable for high-demission grid. The

algorithm is another approach that has been used in stellar codes (e.g. the MESA SIMPLEX module Paxton et al. 2013). It offers an automated likelihood minimisation to search for optimal solutions. This method is statistically-sound and works well for modelling individual stars. However, it is not efficient when modelling a large sample because the algorithm needs to iteratively compute stellar tracks many time for each single star.

Machine learning is being applied to the field of stellar research in many ways to efficiently characterise stars. Verma et al. (2016) applied artificial neural network, which is a series of algorithms that endeavours to recognise underlying relationships in a set of data, to determine the evolutionary parameters of the sun and sun-like stars based on spectroscopic and seismic measurements. Using a similar artificial neural network interference, Hendriks & Aerts (2019) developed a method to provide the optimal starting point of model competitions for more detailed forward asteroseismic modelling. Moreover, Momberg et al. (2021) trained neural networks to predict theoretical pulsation periods of high-order gravity modes, as well as the luminosity, effective temperature, and surface gravity for a given mass, age, overshooting parameter, diffusive envelope mixing, metallicity, and near-core rotation frequency. Using different machine learning tools, Bellinger et al. (2016) trained a random forest regressors(Ho 1995), which is an ensemble learning method

[★] E-mail: t.li.2@bham.ac.uk

[†] E-mail: G.R.Davies@bham.ac.uk

for regression and operates by constructing a multitude of decision trees, to rapidly estimate fundamental parameters of solar-like stars based on classical and asteroseismic observations. Hon et al. (2018) developed a convolutional neural network classifier that analyses visual features in asteroseismic frequency spectra to distinguish between red giant branch stars and helium-core burning stars. Wu et al. (2019) determined masses and ages for massive RGB stars from their spectra with a machine-learning method based on kernel principal component analysis, which is a nonlinear form of principal component analysis using integral operator kernel functions and can efficiently compute principal components in high dimensional feature spaces related to input space by some nonlinear map (Schölkopf et al. 1997). Hon et al. (2020) applied the mixture density network (Bishop 1994), which learns a transformation from a set of input variables to a set of output variable, to determine stars’ fundamental parameters like mass and age based on observed mode frequencies, spectroscopic and global seismic parameters.

In above studies, the discriminative machine-learning model is mostly used. The discriminative model treats observables as given facts to directly infer star fundamental parameters. The method is efficient and easy for computation, while the downside is not allowing any priors for star properties like mass. In an opposite direction, the generative machine-learning model uses the star fundamental parameters as given facts to predict observables. This approach offers flexibility to prior fundamental parameters in the sampling. For instance, Lytle et al. (2021) determined initial helium fraction and mixing-length parameters for a sample of Kepler dwarfs and subgiants with the artificial neural network. The application of the generative model allow them giving either weakly or strongly informative priors while constraining the two fundamental parameters. (*Can Alex add a few sentence to address the advantages of having different priors?*)

Constructing a comprehensive and fine model grid is computationally expensive. In this work, we aim to apply the machine learning tool to transform a sparse model grid onto a continuous function. We apply a machine learning algorithm that involves a Gaussian process (GP) that measures the similarity between data points (i.e., the kernel function) to predict values for unseen points from training data. We use the generative model and treat fundamental parameters as given facts to predict observables. This gives us flexibility to prior fundamental inputs when modelling stars. We organise the rest of the paper as follow. Section 2 contents descriptions about the computation of a representative stellar model grid. We then introduce the underline theory of GP and the setup of GP model in Section 3. Section 5 demonstrates GP predictions and their systematic uncertainties. Subsequently, we augment the grid to have a set of continuously-sampled stellar models and model 100 fake stars for testing the accuracy of our method in Section 6. Lastly, we discuss advantages and limitations of this approach, highlight areas where improvements can be found in the near future, and summary conclusions in Section 7.

2 REPRESENTATIVE MODEL GRID

2.1 Grid computation

We compute a stellar model grid as the training dataset. We aim to cover stars with approximate solar mass on the main-sequence and the subgiant phases. We consider four independent fundamental inputs which are stellar mass (M), initial helium fraction (Y_{init}), initial metallicity ($[\text{Fe}/\text{H}]_{\text{init}}$), and the mixing-length parameter (α_{MLT}).

Table 1. Computation of Stellar model grid.

Primary dataset		
Input Parameter	Range	Increment
$M (M_{\odot})$	0.80 – 1.20	0.01
$[\text{Fe}/\text{H}] (\text{dex})$	-0.5 – 0.2/0.2 – 0.5	0.1/0.05
Y_{init}	0.24 – 0.32	0.02
α_{MLT}	1.7 – 2.5	0.2

Additional dataset		
Input Parameter	Range	Increment
$M (M_{\odot})$	1.055 – 1.195	0.01
$[\text{Fe}/\text{H}] (\text{dex})$	0.25 – 0.45	0.1
Y_{init}	0.25 – 0.31	0.02
α_{MLT}	1.8 – 2.4	0.2

We calculated three model dataset for different purposes. The primary dataset is a standard model grid with uniform mass step. This model grid is used for all preliminary tests and also for the final training. We also calculate an additional dataset to increase the grid resolution for $M > 1.05M_{\odot}$. Because we find that the ‘hook’ feature (where global parameters sharply vary) is relatively hard to train. This dataset is only used in the final training. Details of parameter ranges and steps of the two grid are listed in Table 1. For validating and testing GP predictions, we computed off-grid models with randomly sampled fundamental inputs. The computation of evolutionary tracks starts at the Hayashi line and terminates at the base of red-giant branch (RGB) where $\log g = 3.6$ dex. Note that we only use models after the zero-age-main-sequence (ZAMS), which is defined as the point where core-hydrogen burning contributes over 99.9% of the total luminosity.

2.2 Input physics

We use the stellar code Modules for Experiments in Stellar Astrophysics (MESA, version 12115) to construct stellar grids. MESA is an open-source stellar evolution package which is undergoing active development. Descriptions of input physics and numerical methods can be found in Paxton et al. (2011, 2013, 2015). We adopted the solar chemical mixture $[(Z/X)_{\odot} = 0.0181]$ provided by Asplund et al. (2009). The initial helium fraction (Y_{init}) and initial metallicity ($[\text{Fe}/\text{H}]_{\text{init}}$) are independent inputs. The initial chemical composition is calculated with

$$\log(Z_{\text{init}}/X_{\text{init}}) = \log(Z/X)_{\odot} + [\text{Fe}/\text{H}]_{\text{init}} \quad (1)$$

We use the MESA $\rho - T$ tables based on the 2005 update of OPAL EOS tables (Rogers & Nayfonov 2002) and OPAL opacity supplemented by low-temperature opacity (Ferguson et al. 2005). The grey Eddington $T - \tau$ relation is used to determine boundary conditions for modelling the atmosphere. The mixing-length theory is implemented and the convection is adjusted by the mixing-length parameter (α_{MLT}). We also apply the MESA predictive mixing scheme (Paxton et al. 2018, 2019), which improves model structures at the convective boundary. Atomic diffusion of helium and heavy elements was also taken into account. MESA calculates particle diffusion and gravitational settling by solving Burger’s equations using the method and diffusion coefficients of Thoul et al. (1994). We consider eight elements (^1H , ^3He , ^4He , ^{12}C , ^{14}N , ^{16}O , ^{20}Ne , and ^{24}Mg) for diffusion calculations, and have the charge calculated by the MESA ionization module, which estimates the typical ionic charge

as a function of T , ρ , and free electrons per nucleon from Paquette et al. (1986). The MESA inlist used for the computation is available on https://github.com/litanda/mesa_inlist.

2.3 Equivalent Evolutionary Phase

Apart from the four independent model inputs, i.e., mass, metallicity, helium fraction, and the mixing-length parameter, stellar age is the fifth fundamental input. However, the dynamical range of age varies track by track. This makes GP models hard to map from age to global parameters. We need a uniform input to replace the age. The fractional age is an option but we find that global parameters (e.g. effective temperature) sharply change with the fractional age around the 'hook' and the turn-off point (as shown in the left panel in Figure 1). It requires a complex and spiky kernel function to fit the curvatures in this area and hence difficult for GP to learn. Dotter (2016) has introduced a quantity Equivalent Evolutionary Phase (*EEP*), which numbers evolutionary stages and transform stellar tracks onto a uniform basis. We follow this idea but define *EEP* in a different way to make global parameters change relatively smoothly. On each evolutionary track, we compute the displacement between consecutive models on the T_{eff} – $\log g$ diagram. For instance, the displacement between model n and model $n - 1$ can be calculated as

$$\delta d_n = ((T_{\text{eff},n} - T_{\text{eff},n-1})^2 + (\log g_n - \log g_{n-1})^2)^c, \quad (2)$$

where c is an adjusted parameter to scale the displacement. The total displacement of model n from the ZAMS (model 0) can be calculated with

$$d_n = \sum_{i=0}^{i=n} \delta d_i. \quad (3)$$

We then normalise d_n to the 0 – 1 range and define it as *EEP*. On an evolutionary track, *EEP* equals to 0 at the ZAMS and 1 on the RGB where $\log = 3.6 \text{ dex}$. The factor f in Eq. 2 is introduced for modulating *EEP* to avoid obvious data gap in the parameter space, and we find that $c = 0.18$ gives the most uniform data distribution. In Figure 1, we demonstrate how the effective temperature changes with fractional age and *EEP*. It can be seen that *EEP* is a better choice than the fractional age because global parameters change smoother around the 'hook' and the turn-off point.

2.4 Sampling method

There is a limitation of the data size in the GP framework, because the computational and memory complexity exponentially increase with the number of data points. In practice, the typical data size is on an order of 10^4 . Given that the grid contents $\sim 10,000,000$ stellar models, only a small subset can be used for training. The sampling method is hence critical. A flat sampling is not appropriate, because the evolving step is not uniform at different evolutionary stages due to the MESA step-control strategy. For instance, stellar models are dense at the main-sequence and lower RGB but quite sparse at the subgiant stage. We test a few methods and find that using the displacement (δd_n) defined in Eq. 2 as the weight to sample models on an evolutionary track gives a relatively uniform data distribution at different evolutionary stages.

3 GAUSSIAN PROCESS MODEL

A GP can be applied as a probabilistic model to a regression problem. Here we use the GP model to generalise a stellar model grid to a continuous and probabilistic function that maps inputs to observable quantities. This will allow us to predict observable quantities that are off the grid of stellar models with the prediction including uncertainty. We intend to train GP models that maps five fundamental inputs, i.e., mass (M), initial metallicity ($[\text{Fe}/\text{H}]_{\text{init}}$), initial helium fraction(Y_{init}), the mixing-length parameter(α_{MLT}), and equivalent evolutionary phase (*EEP*), to five model outputs including effective temperature(T_{eff}), surface gravity($\log g$), radius(R), surface metallicity($[\text{Fe}/\text{H}]$), and stellar age(τ). We use the GP model as a non-parametric emulator, that is emulating the comparatively slow calls to models of stellar evolution. This emulator can be described as a function approximation problem. In fact, the way we have implemented the GP as function approximation means that we have used one GP for each of the outputs so that they can be described as

$$T_{\text{eff}} = f_{T_{\text{eff}}} (M, EEP, [\text{Fe}/\text{H}]_{\text{init}}, Y_{\text{init}}, \alpha_{\text{MLT}}), \quad (4)$$

$$\log g = f_{\log g} (M, EEP, [\text{Fe}/\text{H}]_{\text{init}}, Y_{\text{init}}, \alpha_{\text{MLT}}), \quad (5)$$

$$R = f_R (M, EEP, [\text{Fe}/\text{H}]_{\text{init}}, Y_{\text{init}}, \alpha_{\text{MLT}}), \quad (6)$$

$$[\text{Fe}/\text{H}] = f_{[\text{Fe}/\text{H}]} (M, EEP, [\text{Fe}/\text{H}]_{\text{init}}, Y_{\text{init}}, \alpha_{\text{MLT}}), \quad (7)$$

and

$$\tau = f_\tau (M, EEP, [\text{Fe}/\text{H}]_{\text{init}}, Y_{\text{init}}, \alpha_{\text{MLT}}). \quad (8)$$

In the following, we introduce the underline theory of GP regression and the setup of training GP models.

3.1 Gaussian Process Application

In our application to a stellar model grid, a GP has a number of desirable properties. While a GP is a stochastic process, the distribution of a GP can be considered as a distribution of functions with a continuous domain. In fact, the marginal likelihood considered in function space is equal to the likelihood of the data given some function values, multiplied by the prior on those function values marginalised over all function values Williams & Rasmussen (1996). That is to say that, the GP allows for the analytical evaluation of a fit over many different functions (perhaps an infinite number) weighted by some concept of a prior and the agreement with the data. In addition, while the marginal likelihood will be assessed on discrete data, predictions can be made using linear algebra for new data in the continuous domain, but crucially again marginalised over these many different functional forms. It is possible to see how this might be useful for generalising (or emulating or augmenting) a discrete grid of stellar models in order to obtain predictions in the continuous domain.

In this section we will look at the required mathematics to be able to implement a GP for our application to grids of stellar models. We start with a series of definitions before dealing with the marginal likelihood and the posterior predictive distributions.

We start with a grid of stellar models containing N models with a label we want to learn, for example model effective temperature, which we will denote with the general symbol y , and a set of on-grid inputs \mathbf{X} (e.g., mass, *EEP*, metallicity, ...). We can use a GP to make

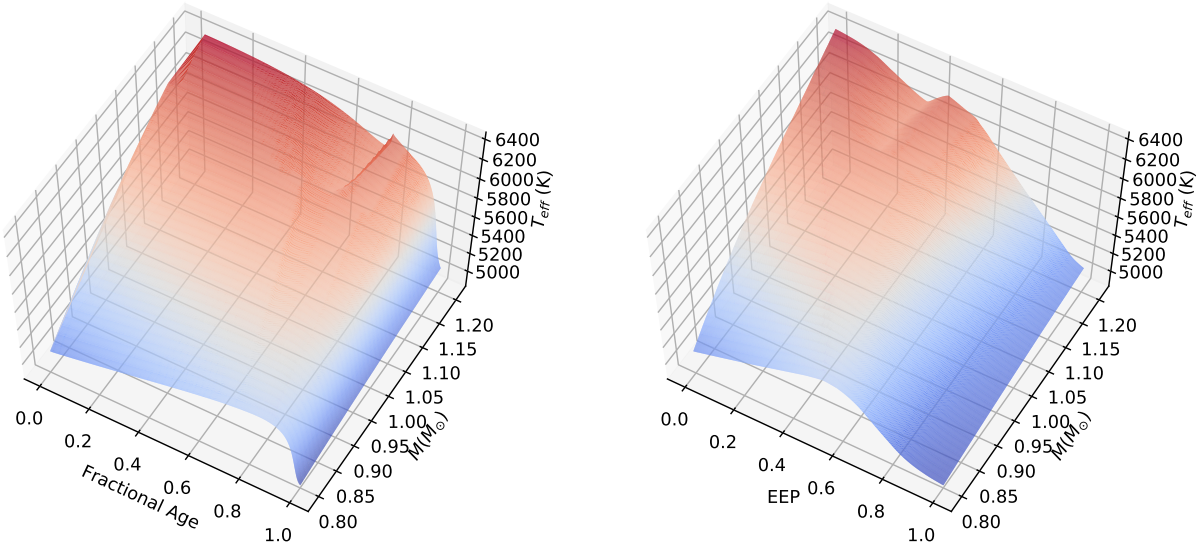


Figure 1. Surface plots of model effective temperature on the mass-fractional age (left) and mass-EEP (right) diagrams. Models in this figure are from the primary grid with fixed initial metallicity ($[Fe/H]_{\text{init}} = 0.0$), helium fraction ($Y_{\text{init}} = 0.28$) and mixing-length parameter ($\alpha_{\text{MLT}} = 2.1$). It can be seen that the effective temperature changes much smoother on the mass-EEP diagram at the hook and turn-off points.

predictions of the effective temperature (labelled y) for additional off-grid input values given by \mathbf{X}_* . The vector \mathbf{y} is arranged $\mathbf{y} = (y_1, \dots, y_N)^T$ where the subscript label references the stellar model. The input labels are arranged into a $N \times D$ matrix where D is the number of input dimensions (e.g., $D = 3$ for mass, EEP , and metallicity) so that $\mathbf{X} = (\mathbf{x}_1, \dots, \mathbf{x}_N)^T$ where $\mathbf{x}_i = (x_{1,i}, \dots, x_{D,i})^T$. The matrix of additional inputs \mathbf{X}_* has the same form as \mathbf{X} but size $N_* \times D$.

Williams & Rasmussen (1996), from which our description below is based, define a GP as a collection of random variables, where any finite number of which have a joint Gaussian distribution. In general terms, a GP may be written so that our on grid labels are random variables drawn from our GP distribution,

$$\mathbf{y}(\mathbf{X}) \sim \mathcal{GP}(m(\mathbf{X}), \Sigma), \quad (9)$$

where $m(\mathbf{X})$ is some mean function, and Σ is some covariance matrix. The mean function controls the deterministic part of the regression and the covariance function controls the stochastic part. The mean function defined here could be any deterministic function and we will label the additional parameters, or hyperparameters, ϕ . Each element of the more familiar covariance matrix is defined by the covariance function or *kernel function* \mathbf{K} which has hyperparameters θ and is given by,

$$\Sigma = \mathbf{K}(\mathbf{X}, \mathbf{X}, \theta), \quad (10)$$

or

$$\Sigma_{n,m} = k(\mathbf{X}_n, \mathbf{X}_m, \theta), \quad (11)$$

where the inputs \mathbf{X}_n and \mathbf{X}_m are D -dimensional vectors and the output is a scalar covariance. In addition to the covariance defined by the kernel function, we include additional white noise in the covariance matrix by adding an identity matrix \mathcal{I} multiplied by a scalar value σ_w^2 , so that,

$$\Sigma = \mathbf{K}(\mathbf{X}, \mathbf{X}, \theta) + \sigma_w^2 \mathcal{I}, \quad (12)$$

where σ_w^2 is another hyperparameter to be learnt in training.

3.1.1 The likelihood

Conceptually we value the GP because of its ability to marginalise over many functions \mathbf{f} and return a marginal likelihood,

$$p(\mathbf{y}|\mathbf{X}) = \int p(\mathbf{y}|\mathbf{f}, \mathbf{X}) p(\mathbf{f}|\mathbf{X}) d\mathbf{f}, \quad (13)$$

noting that this function space marginal likelihood is weighted by the probability of the data given the function and the probability of the function. This integral could be evaluated. However, by noting that a GP is a collection of random variables, where any finite number of which have a joint Gaussian distribution, the marginal probability of our data \mathbf{y} is also the joint likelihood of a multivariate normal distribution,

$$p(\mathbf{y}|\mathbf{X}) = \mathcal{N}(m(\mathbf{X}), \Sigma), \quad (14)$$

which can be straightforward to evaluate. Thus the marginal likelihood is,

$$p(\mathbf{y}|\mathbf{X}) = (2\pi)^{k/2} \det(\Sigma)^{-0.5} \exp\left(\frac{-1}{2} (\mathbf{X} - m(\mathbf{X}))^T \Sigma^{-1} (\mathbf{X} - m(\mathbf{X}))\right), \quad (15)$$

which can be evaluated without integrating over all possible function space. While this marginal likelihood expression is clearly more computationally feasible than the integral over functional space it is not without its limitations. Because it is necessary to calculate the determinant and the inverse of the covariance matrix, typically applied algorithms, make this a $O(N^3)$ or $O(N^2 \log N)$ operation. This naturally limits the size of the data set for which the likelihood, and optimisations of the likelihood, can be applied.

3.1.2 Making predictions

If we want to obtain predictive distributions for the output \mathbf{y}_* given the inputs \mathbf{X}_* , the joint probability distribution of \mathbf{y} and \mathbf{y}_* is

Gaussian and given by

$$p\left(\begin{bmatrix} \mathbf{y} \\ \mathbf{y}_\star \end{bmatrix}\right) = \mathcal{N}\left(\begin{bmatrix} m(\mathbf{X}) \\ m(\mathbf{X}_\star) \end{bmatrix}, \begin{bmatrix} \Sigma & \mathbf{K}_\star \\ \mathbf{K}_\star^T & \mathbf{K}_{\star\star} \end{bmatrix}\right), \quad (16)$$

where the covariance matrices Σ and \mathbf{K} are computed using the kernel function so that,

$$\Sigma_{n,m} = k(\mathbf{X}_n, \mathbf{X}_m), \quad (17)$$

which is an $N \times N$ matrix.

$$\mathbf{K}_{\star n,m} = k(\mathbf{X}_n, \mathbf{X}_{\star m}), \quad (18)$$

which is an $N_\star \times N_\star$ matrix, and finally

$$\mathbf{K}_{\star\star n,m} = k(\mathbf{X}_{\star n}, \mathbf{X}_{\star m}), \quad (19)$$

which is an $N_\star \times N_\star$ matrix. The predictions of \mathbf{y}_\star are again a Gaussian distribution so that,

$$\mathbf{y}_\star \sim \mathcal{N}(\hat{\mathbf{y}}_\star, \mathbf{C}), \quad (20)$$

where

$$\hat{\mathbf{y}}_\star = m(\mathbf{X}_\star) + \mathbf{K}_\star^T \Sigma^{-1} (\mathbf{y} - m(\mathbf{X})), \quad (21)$$

and

$$\mathbf{C} = \mathbf{K}_{\star\star} - \mathbf{K}_\star^T \Sigma^{-1} \mathbf{K}_\star. \quad (22)$$

At point we can make predictions on model properties given a grid of stellar models using equation 20. But these predictions will likely be poor unless we select sensible values for the form and hyperparameters of the mean function and covariance function. In the following section we detail a number of kernel functions that will be tested against the data. We will then discuss the method for determining the values of the hyperparameters to be used.

3.2 Setup of GP Models

3.2.1 Tool package

We adopt a tool package named GPyTorch, which is a GP framework developed by Gardner et al. (2018). It is a Gaussian process library based on an open source machine-learning framework PyTorch (<https://pytorch.org>). The package provides significant GPU acceleration, state-of-the-art implementations of the latest algorithmic advances for scalability and flexibility, and easy integration with deep learning frameworks. Source codes and detailed introductions could be found on <https://gpytorch.ai>. All the trainings are on an NVidia Tesla V100 graphics processing unit (GPU) with 32GB GPU Memory. The GPU captivity allows training up to $\sim 20,000$ data points for a GP model.

3.2.2 Training procedure

The training procedure of a GP model includes training, validating, and testing. In the training process, we iteratively optimise hyperparameters of a GP model to learn the underline function which maps inputs to outputs from on-grid evolutionary tracks (training dataset). In each iteration, the GP model is validated by comparing true and GP predicted values of off-grid tracks (validating dataset). Although the validating dataset is not directly involved in training hyperparameters, it still constructs the GP model to some extend because the optimal solution is the one that best fits the validating dataset. For this reason, the validating dataset does not give a completely independent validation for a GP model. We hence have a

testing process at the end. We do this by reserving a half of off-grid tracks from the training and validating process. These tracks (testing dataset) are used to estimate the systematic errors/uncertainties of GP model.

Here we briefly summary the setup of GP model training. We apply an architecture Neural Network including 6 hidden layers and 128 nodes per layer as the mean function. The GPyTorch standard likelihood for regression, which assumes a standard homoskedastic noise model, is used as the likelihood function, and we the negative logarithm of the likelihood as the loss function. The optimiser for training is called ‘Adam’, which is a combination of the advantages of two other extensions of stochastic gradient descent, specifically, Adaptive Gradient Algorithm and Root Mean Square Propagation. To avoid overfitting, we set up an Early Stopping by monitoring the validating errors. The training is terminated when there is no improvement in validation error for 300 iterations. The GP model is saved when the so-far best validation result is found. Detailed discussions about these setup can be seen in the Appendix A.

3.2.3 Kernel Function

To select the proper kernel function for training GP models, we test four basic kernels and a number of combined kernels. The four basic kernels are listed as follow.

- **RBF:** Radial Basis Function kernel (also known as squared exponential kernel)
- **RQ:** Rational Quadratic Kernel (equivalent to adding together many RBF kernels with different lengthscales)
- **Mat12:** Matern 1/2 kernel (equivalent to the Exponential Kernel)
- **Mat32:** Matern 3/2 kernel

These four kernels are all universal, and we can integrate each of them against most functions. Every function in its prior has infinitely many derivatives. The differences between these kernels can be simply understood as their different smoothness and complexity. The RBF kernel is very smooth and suits for the case when the data follow a slowly varying function. The RQ kernel, as a combination of many RBF kernels, is more complex and is able to fit to data with a number of smooth underline functions (e.g. when the output depends on some inputs in different ways). One the opposite, the Mat12 kernel is very spiky and it can fit any sharp variations in the data. The Mat32 kernel has a smoothness somewhere between the RBF and Mat12 kernels. It is a smooth function but has significantly more extrema than the RBF kernel. These differences are not chance coincidence, and the origin of these differences are crucial for interpreting the results. Choosing a good kernel for a particular application is necessary for good predictions. If the generates functions that are too spiky, then the analysis will have variance that is too high. On the contrary, if the kernel function is too smooth, it may not fully capture the variability of the underlying function and lead to an increase in bias. Combining basic kernels can increase the complexity or flexibility of kernel function. For instance, the combination of a RBF kernel and a Mat12 kernel is able to fit to both smooth and spiky features in the data. However, the risk of using combined kernel (increasing the complexity or flexibility of kernel function) is overfitting.

According to the stellar theory, changing fundamental input parameters smoothly changes the dependent outputs. Hence the kernel function for our application needs to be smooth. Moreover, we can notice in Figure 1 that the observable quantities fast vary at some particular regions (e.g., around the ‘hook’). This means

that a slowly varying function like the RBF kernel may under fit in these areas. We do a number of preliminary studies of training GP models with different kernel functions to choose the proper kernel function. Details of training will be mentioned in Section 4.2. Here we only summary the results. We apply four basic kernels and a number of their combinations (RBF + Mat21, RQ + Mat21, Mat32 + Mat21, RBF + Mat32, RQ + Mat32) to train GP models, and then test GP predictions with off-grid models which are not involved in the training. The combined kernel RBF+Mat21 gives the best fit to the training data, however, its testing errors are large. This indicates that the kernel is too flexible and hence overfits to the data. The kernel having the best performance is the Mat32. The GP model with Mat32 fits training data reasonably well and gives the best predictions for the testing models. The results match our expectations. What we need is a smooth function but not too smooth to fit to the quick variations at some particular evolutionary phases. The Mat32 kernel is apparently suitable for our application.

4 PRELIMINARY STUDIES

Before training the whole model grid (with five input demissions), we start with a number of preliminary studies on low-demission dataset. These preliminary studies are for several purposes. In the 1D problem (training data on a single evolutionary track), we compare GP predictions with the classical interloper using the quadratic function. In the 2D problem, we train GP models on a mass – *EEP* platform to test the performances of using different kernel functions. We also discuss about introducing a new error index to validating and testing GP models instead of using a global error quantity such like Root Mean Square Error. In the 3D problem, where GP maps three fundamental inputs (mass, EEP, and metallicity) to observables, we solve the training strategy for large dataset whose data size excesses the practical limitation of a GP model.

4.1 1D Problem

We first demonstrate an example of GP application on an 1D problem. We train a GP model using the Mat32 kernel to learn the evolution of effective temperature for a $1.1M_{\odot}$ track. We split the model data points on this track into training and testing data by 70-to-30. We train a GP model which maps *EEP* to effective temperatures and then compare GP-predicted effective temperatures with truths. As it can be seen in Figure 2, the GP model gives very good predictions with all residuals less than ± 0.5 K. As a comparison, we fit the training data with the quadratic function and use it to do the same predictions. As it shown that we find very similar results from the two methods. It suggests that GP can be an alternative of classical interpolators on the 1D problem.

4.2 2D Problem

As a further step, we train GP models for the 2D problem where GP models map mass and *EEP* to the five observable outputs (Outputs = $f(M, EEP)$). Training data are selected from the primary grid with fixed $[Fe/H]_{init}$ (0.0), Y_{init} (0.28), and α_{MLT} (2.1). There are 41 evolutionary tracks which content 24,257 models, and we sample 20,000 of them. To validate and test GP models, we compute 44 evolutionary tracks with the same $[Fe/H]_{init}$, Y_{init} , and α_{MLT} but random M . We split the off-grid track half-to-half as validating and testing datasets. Our code for training is developed based on the SIMPLE GP REGRESSION exam-

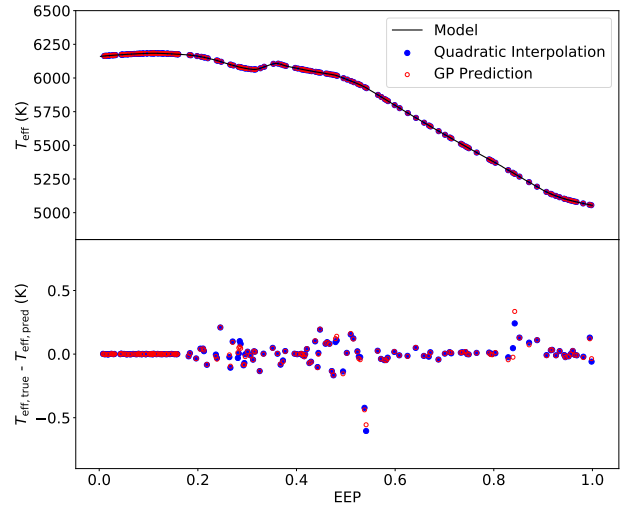


Figure 2. GP application on 1D problem. Models on this track are split into training and testing data by 70-to-30. Top: the evolution of effective temperature for a $1.1M_{\odot}$ track. The grey line is the evolutionary track computed with MESA; blue and red circles indicate predictions for the testing data from the quadratic interpolator and the GP model. Bottom: residuals of predictions in the top graph.

ple (https://docs.pytorch.ai/en/stable/examples/01_Exact_GPs/Simple_GP_Regression.html). We change the mean function and optimiser in the example and add an early stopping and a model saving modules. The script used for the training this 2D problem can be seen at [somewhere-at-github](#). We follow the aforementioned training procedure to train, validate, and test GP models. We illustrate the GP model (with the Mat32 kernel) for effective temperature on the mass–*EEP* diagram in Figure 3. As it shown that, GP transforms the sparse data into a continuous function and hence is able to predict values for unseen points in the grid.

It can be seen in Figure 3 that the kernel function in the area of $M \geq 1.05M_{\odot}$ and $EEP \leq 0.7$ is more complex than that for other regions. This particular area are relatively difficult to learn and poorly predicted by the GP model. There are two regions where global parameters vary relatively fast. The first is around the ‘hook’ and main-sequence-turn-off point ($EEP \sim 0.4$) where high-mass tracks sharply turns on the HR diagram. The second is at early subgiant phase ($EEP \sim 0.6$) where stars fast restructure. When there is a subregion in which the GP model performs worse than other areas, the error distribution would not follow a Normal function. As shown at the bottom of Figure 3, the density distribution of testing errors form long tails which contents about 10% data. We inspect testing errors for other four outputs. The cases of surface gravity and radius are similar to the effective temperature. The region where the surface metallicity quickly changes is not at the hook but at the early subgiant phase in relatively high-mass tracks. This is because high-mass models maintain shallow convective envelope and hence have strong diffusion effect during the main-sequence stage. At the early subgiant phase, the quick expansion of the surface convective envelope mixes up the settled heavy elements, leading to a fast raise of the surface metallicity. We also find that the accuracy of age prediction drops down for very old low-mass stellar models. This is because age values vary in a relatively big dynamic range (15 –

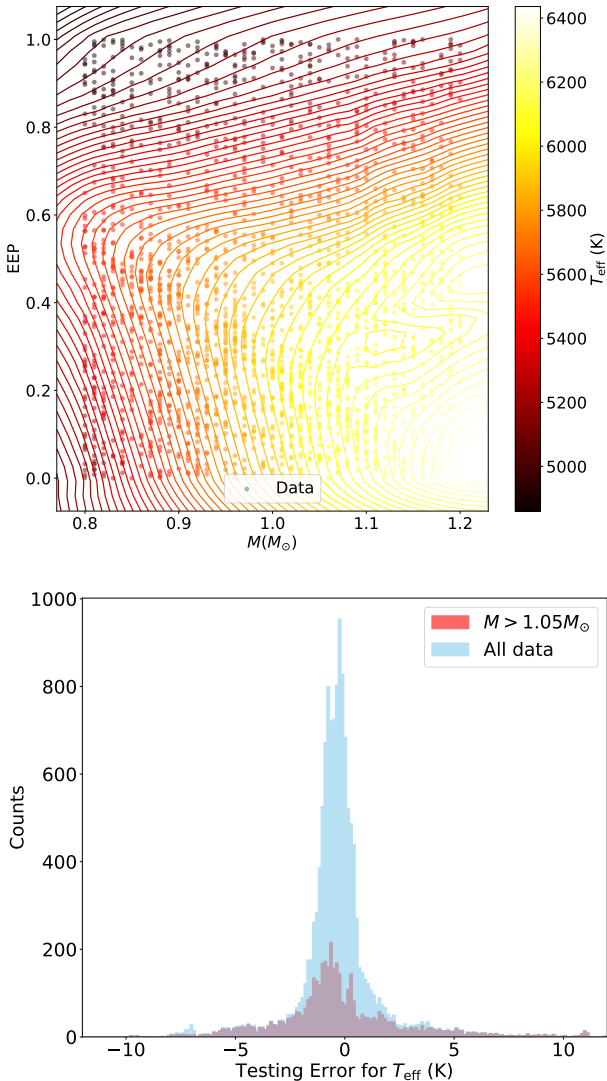


Figure 3. Top: The 2D GP model for T_{eff} . Bottom: probability distributions of validating errors of the GP model.

50 Gyr) in a small fraction of data points. Poor GP predictions are caused by the low age resolution.

The error distribution causes an issue in validating and testing GP models. In the training process, we normally use some global errors, such like Root Mean Square Error (RMSE), to represent the validation or testing results. For this case, a global error indicates the general accuracy but is not able to point out how GP performs in the regions where an observable quantity quickly varies. We hence want to have an error index that can reflect the GP model performance in those sub-areas. By inspecting the error distributions of all five outputs, we find the data points in the tails (outside the 3 times of full width at half maximum) are around 10% (8 - 12% for different outputs). For the majority (90%) of data points, which from a Gaussian-like profile, the 68% confidential interval ($1-\sigma$ uncertainty) can be used to reflect the global accuracy. For the worst 10% of the data, we could use the 95% and 99.7% confidential intervals (2- and 3- σ uncertainties) to describe the median and the length of the tail. Thus, we define an Error Index (EI), which is the sum of 68%, 95%, and 99.7% cumulative values of the absolute

errors. For the case in Figure 3, cumulative values at 68%, 95%, and 99.7% are 1.1, 4.9, and 11.1K, which give a testing EI equals to 17.1K. We apply this EI in all following training processes to validate and test GP models.

We train GP models using different kernel functions to investigate which is the best for our application. We do this with the 2D data because the training is fast to be able to test many different options. As mentioned in Section 3.2.3, we find Mat32 is the most suitable kernel for mapping the stellar model grid.

4.3 3D Problem: Strategy for Large Data Sample

We apply GP to a 3D problem where GP maps three fundamental inputs, i.e., mass, EEP, and metallicity to five observables. The main purpose of this preliminary study is investigate the strategy for training large data sample exceeding the data size limitation. We select training data from the primary grid with $Y_{\text{init}} = 0.28$ and $\alpha_{\text{MLT}} = 2.1$. The training dataset contents $\sim 300,000$ data points which is 15 times the limit of training data size (20,000). For validating and testing purposes, we compute another 174 evolutionary tracks with the same input Y_{init} and α_{MLT} but random input M and $[\text{Fe}/\text{H}]_{\text{init}}$.

We start with sampling only 20,000 training data from the 3D model grid to train GP models. We use the testing EI of these models as standard references. For instance, the testing EI for T_{eff} is 23.5K (2.0, 5.8, and 15.7 K at 68th, 95th, and 99.7th). We then apply two state-of-the-art approaches designed for large dataset to train the model. These two approaches are named as Stochastic Variational GP (SVGP) and Structured Kernel Interpolation (SKI GP). We find some minor improvements in the GP predictions. Comparing the testing EI for T_{eff} , SVGP gives a results of EI = 24.1K (2.2, 6.8, and 15.1K at 68th, 95th, and 99.7th) and SKI GP ends up with EI = 22.9K (2.0, 6.1, and 14.8K at 68th, 95th, and 99.7th). Details about these two implements and some discussions about the results can be seen in appendix B. However, later tests on 5D data show that these two methods can not significantly improve the GP performances, and we hence seek other methods for better training GP models.

The GPU memory captivity limits the actual number of data that induce the kernel function. This limitation becomes critical for the high-demission applications because we need much more data give the fact that the parameter space exponentially increase with input demission. A simple way to overcome this issue is breaking the grid into many sections and train GP models for each section separately. We divide the training dataset into 10 equal sections by EEP and sample 20,000 training data in each. A set of GP models are then trained for each EEP section. Using this section scenario, we improve the testing EI for the five output parameters by around 10%. For instance, the testing EI for T_{eff} decreases from 23.5 to 21.6K. (1.7, 5.0, 14.9K at 68th, 95th, and 99.7th). EI values for the five outputs before and after sectioning the training dataset can be seen in Table 3. On this 3D problem, the section scenario performs slightly better than the SVGP and SKI GP, but it makes more significant improvements in training the 5D dataset, where the SVGP and SKI GP approaches become less reliable for high-demission problems. We hence apply this section scenario as our training strategy.

The section scenario improves the performance of GP model, but there is a major concern about the edge effect at the boundary between segments. If the GP model works significantly poorly at these boundaries, it will be difficult to map the systematic errors across the whole parameter space. We hence examine potential edge effects as illustrated in Figure 4. We inspect absolute testing errors for each output on the $M - \text{EEP}$ diagram. No obvious edge effect

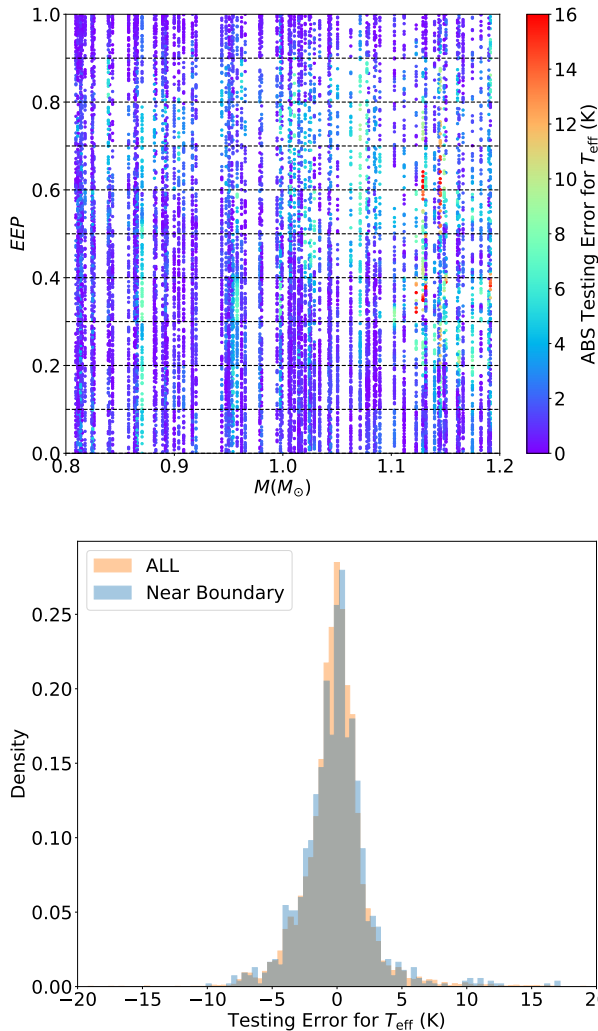


Figure 4. Top: Testing errors of 3D GP model for T_{eff} on the $M - EEP$ diagram. Dashes indicates section boundaries. Bottom: examination of the edge effects of the section scenario. Probability distributions of testing errors of all testing data and those near the boundary ($\pm 0.01 \text{ EEP}$) in the upper graph are compared. As it can be seen, testing errors do not raise around the boundary.

is found. We also do a statistical comparison between all errors and those around section boundaries ($\pm 0.01 \text{ EEP}$). As shown in the bottom graph, the density distributions of the two samples are very similar to each other. We hence adopt the section scenario as our training strategy.

5 AUGMENTING THE STELLAR GRID

Based on preliminary studies, we apply GP to mapping the whole 5D model grid. The setup of GP model is summarised in Table 2. The training data are selected both primary and additional girds as shown in Table 1. Having the additional grid increases the grid resolution for relatively high-mass models, and this gives more information about the fast variation at the ‘hook’ for GP to learn. The training data includes $\sim 15,000$ evolutionary tracks ($\sim 10,000,000$ stellar models). We also computed 4,880 off-grid tracks. These

Table 2. Setup of GP Models

GP model inputs		
Parameter	Notation	Range
Mass	M	$0.8 - 1.2 M_{\odot}$
Equivalent evolutionary phase	EEP	$0 - 1$
Initial metallicity	$[Fe/H]_{\text{init}}$	$-0.5 - 0.5 \text{ dex}$
Initial helium fraction	Y_{init}	$0.24 - 0.32$
Mixing-length parameter	α_{MLT}	$1.7 - 2.5$
GP model outputs		
Parameter	Notation	Trust-worth range ^a
Effective temperature	T_{eff}	$\leq 7000 \text{ K}$
Surface gravity	$\log g$	-
Radius	R	-
Surface metallicity	$[Fe/H]$	$\geq -0.6 \text{ dex}$
Stellar age	τ	$\leq 20 \text{ Gyr}$
Setup of training		
Item	Adopted	
Kernel	Mat32	
Mean Function	6 layers x 128 notes Neural Network	
Likelihood Function	Gaussian Likelihood Function	
Loss Function	Exact marginal likelihood	
Optimiser	Adam including AMSGRAD variant	
Termination	Early Stopping (monitoring the validating EI)	

^a The ranges without strong edge effects.

off-grid tracks are split by 50-to-50 for validating (in the training progress) and testing (after the training progress) GP models. The section scenario is applied. For each section, we train a set of GP models for each output parameter with 20,000 training and 20,000 validating data. The number of sections need to be tested to obtain the best efficiency. To do this, we gradually increase the number of sections from 1 to 100 and track down the changes in testing EI. We find that testing EI is significantly improved from 1 to 5/10 sections but not obvious for more than 10 sections. It turns out that dividing the grid into 10 sections is the most efficient. We hence take GP models for this case as our final results. All following analysis and discussion are based on it. We list the testing EI with different numbers of sections in Table 3. When testing GP models, we do not section the dataset because the data size limitation for testing is not strict. We sample 100,000 data points from the testing dataset. Note that we do not use models with $\tau \geq 20.0 \text{ Gyr}$, $[Fe/H]_{\text{surf}} \leq -0.6 \text{ dex}$, or $T_{\text{eff}} \geq 7000 \text{ K}$ in testing dataset because we find strong edge effects in those ranges.

5.1 Overview of Results

A overview of testing errors (Truths - GP predictions) can be seen in Figure 5, where we plot rolling medians and rolling standard deviations for all outputs’ errors against fundamental inputs. Median values are approximate along zero in most plots, indicating good agreement between GP predictions and true values. The 68% confidential intervals are generally small and their dynamical ranges do not significantly vary across the parameter range. In general, we could conclude that GP predictions are accurate and have good precision compared with typical observed uncertainty. However, it can be noticed that the 95% confidential intervals show more significant changes. The different behaviour between the 68% and 95% confi-

dential intervals are due to the tail feature as seen in Figure 3. Because GP predictions are relatively poor in some particular regions. For instance, predictions for the effective temperature are more scattered in high-mass because of the appearances of the ‘hook’. From these results, we can see that the model systematic uncertainty is not uniform across the parameter space. Proper estimates of model uncertainty are hence necessary.

5.2 Mapping Systematic Uncertainties

When we use a learned GP model to predict, it supposes to give proper uncertainties of predictions. In our preliminary studies, the uncertainties are properly determined for the 1D and 2D problems comparing with the testing errors. However, we notice obvious underestimated uncertainties in the 3D problem. In the final training for the 5D grid, we also find significantly small uncertainties in GP predictions for the testing data: they are mostly one order of magnitude smaller than true errors. It looks that the learned GP models are over-confident in high-demission problem. The reason may be that GP turns to use large lengthscale values to fit to equally spaced data, from which machine-learning tools can not capture small-scale features. (**Guy, could you add some more explanations.**)

In this section, we discuss using testing errors to estimate the systematic uncertainty of GP predictions. As shown in Figure 5, systematical uncertainties relate to M , EEP , and $[Fe/H]_{init}$ but not to Y_{init} or α_{MLT} . Hence, we can treat this as a 3D problem, where we describe GP model systematic uncertainty as a function of M , EEP , and $[Fe/H]_{init}$. We use learned GP model to predict observable quantities for the testing dataset and then calculate testing errors. We inspect the error distributions and find that their local medians smoothly vary in the M - EEP - $[Fe/H]_{init}$ space. For instance, the local T_{eff} errors are generally stable at low-mass range and increase in high-mass range near the ‘hook’ and turn-off points.

We intend to train another set of GP models to map the errors for each outputs. Because the data size is about 100,000 and the underline function is relatively smooth, the SVGP approach is suitable (see Appendix B for detailed discussions about SVGP). We split the data by 75-to-25 for training and validating. We use a constant mean function and the RBF kernel because the data distribution is smooth. The variational evidence lower bound (ELBO) is adopted as the loss function because it is designed for when there is too much data for the exact inference. We set up Early Stopping by tracking the RMSE value of validating data and terminate training when the RMSE value stops decreasing for 100 iterations. The outputs of GP models are the local median of testing errors for five observable quantities and we use them as the systematic uncertainties (referred as $\sigma_{T_{eff}}$, $\sigma_{\log g}$, σ_R , $\sigma_{[Fe/H]_{surf}}$, and σ_τ). To differentiate these learned models, we refer to them as GP-SYS models.

In Figure 6, we compare the actual local systematic uncertainties for T_{eff} at $[Fe/H]_{init} \approx 0.0$ with those given by the GP-SYS models. It shows that the GP-SYS model well reproduces the $\sigma_{T_{eff}}$ distributions. Here the validating errors can be used to examine GP-SYS models. Their average values for all five parameters are small enough to neglect. They are 0.15K for $\sigma_{T_{eff}}$, 0.00008 dex for $\sigma_{\log g}$, 0.0002 R_\odot for σ_R , 0.0009 dex for $\sigma_{[Fe/H]_{surf}}$, and 0.002 Gyr for σ_τ .

6 MODELLING STARS WITH GP PREDICTIONS

6.1 Augmenting the model grid

Now we are able to predict observable outputs with GP models to augment the original stellar grid. We randomly sample 5,000,000 data points with uniform distribution for the give inputs (M , EEP , $[Fe/H]_{init}$, Y_{init} , and α_{MLT}). We then predict five outputs and their systematic uncertainties (with GP-SYS models). This GP-based model dataset can be downloaded at [a-place-for-data](#). In Figure 7, we demonstrate models from the original grid, GP predictions, and the systematic uncertainties on the Kiel diagram. As it shown, the GP models transform the sparse model grid into continues functions.

6.2 GP-based Modelling for 1,000 Fake Stars

As a final test of our method, we use GP-predicted stellar models to characterise 1,000 fake stars to examine whether GP recovers the true observables. We compute 1,000 fake model stars with the same input physics and randomly sampled input fundamental parameters. To avoid the edge effect, fake stars are computed in the range of $T_{eff} = [4700K, 6800K]$, $\log g = [3.7, 4.6]$, $[Fe/H]_{surf} = [-0.35, 0.35]$, $M = [0.85, 1.15]$, $EEP = [0.05, 0.95]$, $Y_{init} = [0.25, 0.31]$, and $\alpha_{MLT} = [1.8, 2.4]$. We use four observables, i.e., T_{eff} , $\log g$, R , and $[Fe/H]_{surf}$, as observed constraints for the modelling. We apply typical observed uncertainty that is $\pm 50K$ for T_{eff} (high-resolution spectroscopy), ± 0.005 dex for $\log g$ (seismology), 3% for R (seismology), and ± 0.05 dex for $[Fe/H]_{surf}$ (high-resolution spectroscopy). Observed value for each constraint is calculated with true value plus a random noise which follows a Gaussian distribution.

We fit fake stars using the Maximum Likelihood Estimate (MLE) method. Note that the variance term in the MLE function contents observed and model systematic uncertainties that determined with GP-SYS models ($\sigma^2 = \sigma_{obs}^2 + \sigma_{sys}^2$). We measure the 16th, 50th, and 84th percentiles of likelihood distribution to estimate a parameter and its uncertainty. We present results for a representative fake star in Figure 8. Observed constraints for this fake star are $T_{eff} = 4926 \pm 50K$, $\log g = 4.536 \pm 0.005$, $[Fe/H]_{surf} = 0.34 \pm 0.05$, and $R = 0.829 \pm 0.025R_\odot$. True fundamental parameters are $M = 0.861M_\odot$, $\tau = 10.8$ Gyr, $[Fe/H]_{init} = 0.403$, $Y_{init} = 0.281$, and $\alpha_{MLT} = 2.356$ (blue dashes). We also fit with the original model grid for comparing. As it shown that the GP-based modelling has a completed statistical sampling and hence gives more sensible posterior distributions than the grid-based modelling. The improvement for the age is obvious. The age determined with the grid does not actually converge because of the under sampling. It infers an age of $7.7^{+3.2}_{-4.2}$ Gyr. This estimate is less accurate and precise than that determined with GP models ($8.3^{+2.6}_{-2.8}$ Gyr). For initial metallicity, initial helium fraction, and the mixing-length parameter, GP-based modelling makes it possible to properly estimate their uncertainty without computing a very fine model grid. The comparison clearly shows that GP is an efficient tool to augment a typical stellar model grid and hence overcome the under sampling issue, as a result, improves the precision of estimate.

We compare inferred mass and age with truths to examine the accuracy of GP-based modelling in Figure 9. Good consistence is found. We can also see that mass and age differences nicely follow a normal distribution, saying that the fitting is only affected by random noises in observations. As companions, we illustrate results from the grid-based modelling in Figure 9 as well. The results for the mass is very similar. However, the centre of distribution shifts by

Table 3. Training and validating errors for GPR Models

Model Type	Inputs	NTraining	Sampling rate	Testing Errors (at 68/95/99.7%)				
				T_{eff} (K)	$\log g$ (10^{-3} dex)	R ($10^{-3} R_{\odot}$)	$[Fe/H]_{\text{surf}}$ (10^{-3} dex)	τ (10^{-2} Gyr)
GP	2D	20,000 x 1	96%	1/5/11	1/3/8	2/6/14	0.5/2/12	1/3/9
GP with 10 sections	3D	20,000 x 1	5%	2/6/16	1/4/10	3/7/17	2/6/22	2/7/22
	3D	20,000 x 10	50%	2/5/15	1/4/11	2/7/17	1/3/20	2/6/19
GP	5D	20,000 x 1	0.2%	3/9/34	2/5/18	4/11/36	2/7/30	3/9/27
GP with 3 sections	5D	20,000 x 3	0.6%	3/8/27	2/5/18	3/7/26	1/4/24	3/7/22
GP with 5 sections	5D	20,000 x 5	1%	2/7/25	1/4/15	3/7/24	1/4/21	2/6/22
GP with 10 sections	5D	20,000 x 10	2%	2/7/27	1/4/14	2/7/26	1/4/20	2/6/21
GP with 20 sections	5D	20,000 x 20	4%	2/7/26	1/4/14	2/7/27	1/3/18	2/6/22
GP with 100 sections	5D	20,000 x 100	20%	2/7/25	1/4/14	2/7/26	1/3/17	2/6/18

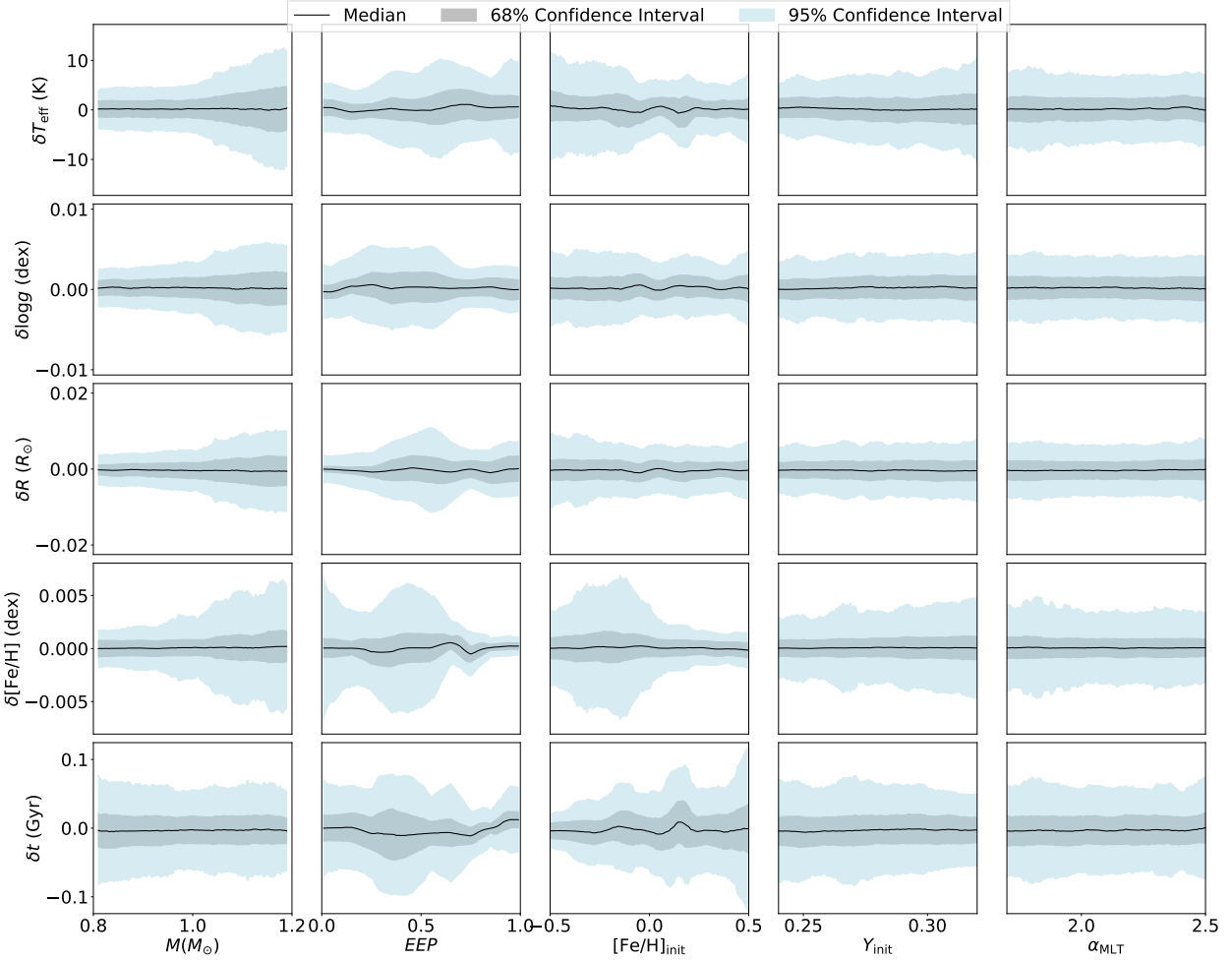


Figure 5. Roll medians and 68/95% confidential intervals of testing errors against GP model inputs. Black solid lines indicate the median value; grey and blue shadowes represent the 68% and 95% confidential interval. Testing errors of T_{eff} , $\log g$, and R mainly depend on M and EEP . Metallicity error strongly depends on M , EEP , and $[Fe/H]_{\text{init}}$, and age error has a significant correlation to EEP and $[Fe/H]_{\text{init}}$. However, testing errors do not obviously relate to Y_{init} or α_{MLT} .

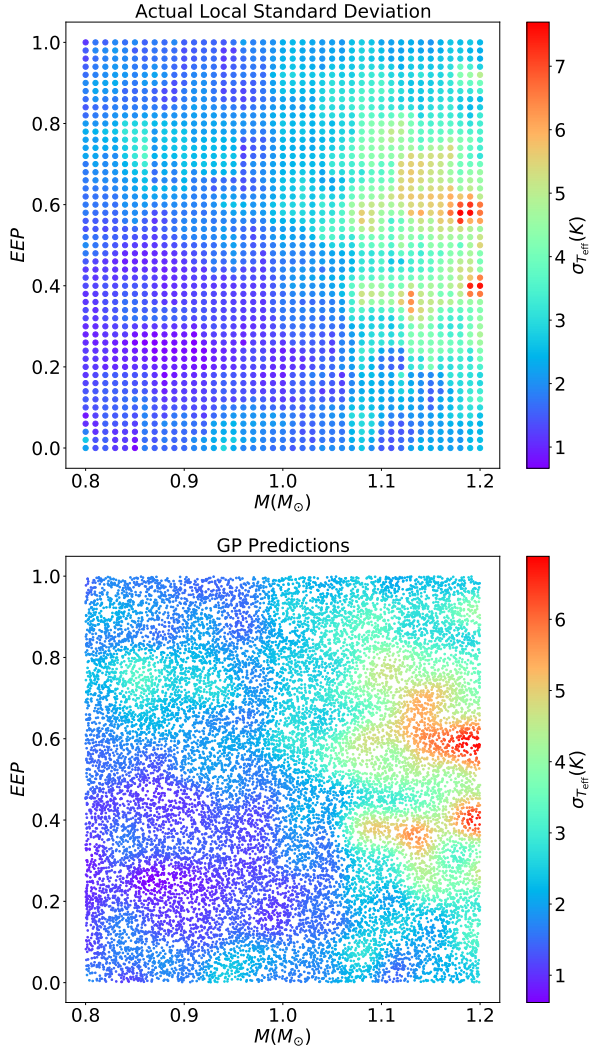


Figure 6. Comparison between actual and GP predicted local systematic uncertainties ($1-\sigma$) for T_{eff} on the $M - \text{EEP}$ diagram at $[\text{Fe}/\text{H}]_{\text{init}} \approx 0.0$. To calculate the actual local values, we separate the mass range into 40 equally-spaced segments and the EEP range into 50, and then measure the median testing error for each segment.

-0.2 for the age. This consists with what is shown in Figure 8. The grid-based modelling can underestimate the age to some extend. We hence conclude that GP-based modelling can give better estimates for stellar properties.

7 DISCUSSION AND CONCLUSIONS (WORK WITH GUY)

In this work, we apply a machine-learning algorithm that involves a Gaussian process for the purpose of augmenting a stellar grid. We train GP models for the stellar grid and obtain continuous functions that map fundamental inputs to observable outputs on a good accuracy level. We also train another set of GP models which describe the local systematic uncertainty of each output parameter. A GP-trained model set is then generated and we use it to model fake stars. The GP-based modelling is obviously advanced in modelling individual stars compared with the gird-based modelling because it provides

continuous sampling. We lastly test GP-determined masses and ages by comparing them with true values and find good consistence.

Advantages

GP is a very efficient tool to augment a stellar grid instead of computing massive evolutionary tracks. For the case in this study, we train 10 GP-Grid models and 1 GP-SYS model for each output parameter and hence 55 GP models in total. The training process takes approximate one hour per GP model on a NVidia Tesla V100 graphics processing unit (GPU). We also show that GP is able to manage the augmentation in high-demissions data (5 demissions in this work), which is very difficult for the interpolation approach. Moreover, the section scenario overcomes the limitation of training data size (20,000 for this case) and offers flexibility to apply GP on stellar grids with different size. When modelling individual stars, GP significantly improves the sampling especially for initial metallicity, helium fraction, and the mixing-length parameter, which are always well spaced in a stellar grid.

Any more points?

Limitations

GP is efficient for training global parameters but not for training the stellar structure. It hence not able to replace a stellar model. To obtain comprehensive stellar model, an optimal path would be using GP to constrain the range of fundamental parameters and then computing models with stellar code in that range.

add more limitations

Future works

This work presents an application of GP on augmenting the whole grid. However, this method is not efficient when modelling a single star. Our future work is developing a fast tool that only trains a small set of models in the grid around a star. This trained-GP model can be easily stucked with an Markov chain Monte Carlo simulator for a delicate bayesian analysis.

more future works

ACKNOWLEDGEMENTS

Development of GPyTorch is supported by funding from the Bill and Melinda Gates Foundation, the National Science Foundation, and SAP.

APPENDIX A: SETUP OF GP MODEL TRAINING

This section includes detailed discussions about the selections of mean function, likelihood and loss function, optimiser, and early stopping.

A1 Mean Function

We first investigate the mean function. As discussed above, the data distribution is generally smooth but complex in some regions of parameter space (e.g., the sub-giant hook). Although a GP model can cope with different mean functions, because of the flexibility of kernels, we find that using a constant or a linear mean function leads to a long time for training. For this reason, we apply a Neural

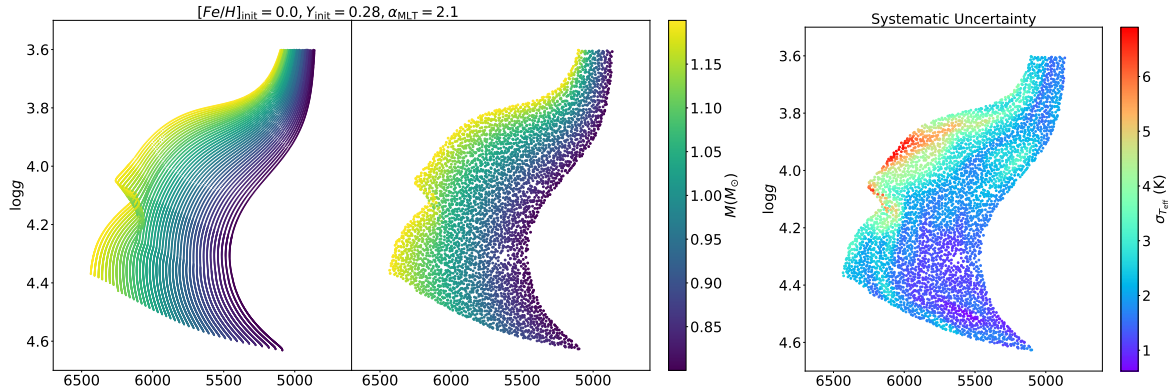


Figure 7. Left: Comparing the original grid and GP predictions on Kiel diagram. Right: The systematical uncertainties for T_{eff} given by GP-SYS models.

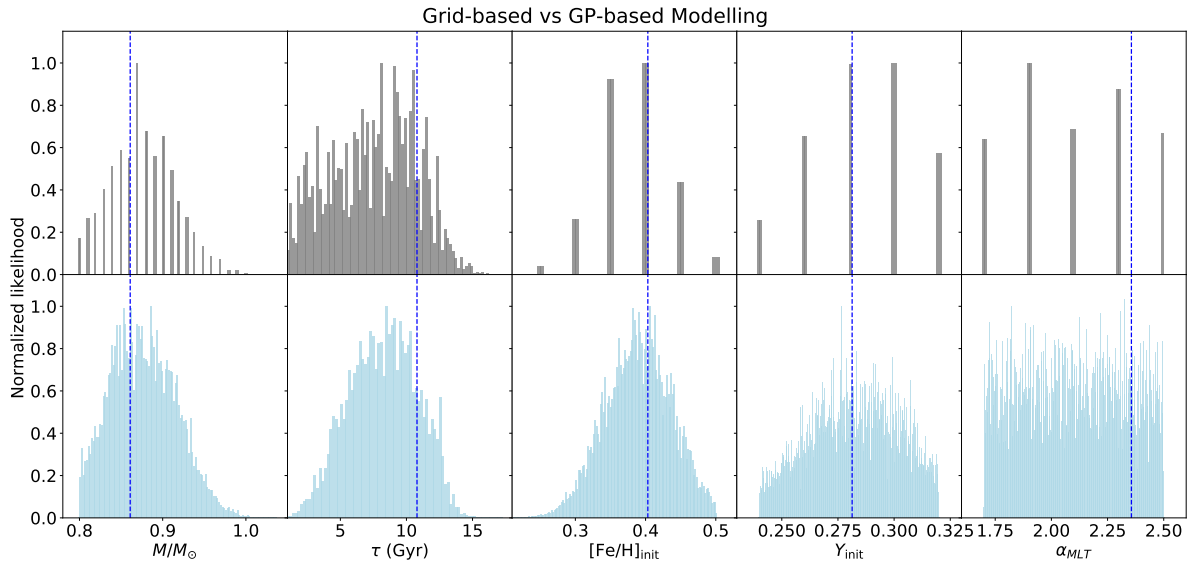


Figure 8. Tanda will add a third row with KDE plots Probability distributions of estimated fundamental parameters from grid-based (Top) and GP-based modelling (Bottom) for a fake star. Observed constraints for this fake star are $T_{\text{eff}} = 4926 \pm 50$ K, $\log g = 4.536 \pm 0.005$, $[Fe/H]_{\text{surf}} = 0.34 \pm 0.05$, and $R = 0.829 \pm 0.025 R_{\odot}$. True values of fundamental parameters are $M = 0.861 M_{\odot}$, $\tau = 10.8$ Gyr, $[Fe/H]_{\text{init}} = 0.403$, $Y_{\text{init}} = 0.281$, $\alpha_{MLT} = 2.356$, which are represented by blue dashes.

Network mean function which is flexible enough to manage both simple and complex features. We adopt an architecture including 6 hidden layers and 128 nodes per layer. All layers apply the linear transformation to the incoming data. We apply the element-wise function (Elu) because it give relatively smooth mean functions. **(Can Guy or Alex add some references for NN and Elu here? The referee may ask why the 6x128 architecture is sufficient, so should we mention Alex's paper?)**

A2 Likelihood and Loss Function

Our training dataset is a theoretical model grid, hence there is no observed uncertainty for each data point, but a tiny random uncertainty exists due to the approximations in the MESA numerical method. We model this using σ_w . This noise model is then assumed to be a Gaussian function with a very small variance. A likelihood specifies the mapping from input values $f(X)$ to observed labels y .

We adopt the standard likelihood for regression which assumes a standard homoskedastic noise model whose conditional distribution is

$$p(y|f(x)) = f + \epsilon, \epsilon \sim \mathcal{N}(0, \sigma^2), \quad (\text{A1})$$

where σ is a noise parameter. We used a small and fixed noise parameter and run a few tests. However, the strict noise parameter makes GP models hard to converge. When this noise parameter is set as free, it reduces to a small value anyway in the training progress because it is data-driven. For this reason, we did not put strict constraint for or prioritise this noise parameter. In practice, we only set up a loose upper limit ($\sigma < 0.1$) to speed up the training. One thing should be noted that a GP model with a large noise parameter is not a proper description for the stellar grid. Because of this, we only adopt GP models with $\sigma \lesssim 10^{-4}$. We train GP models model using the negative logarithm of the likelihood function as the loss function.

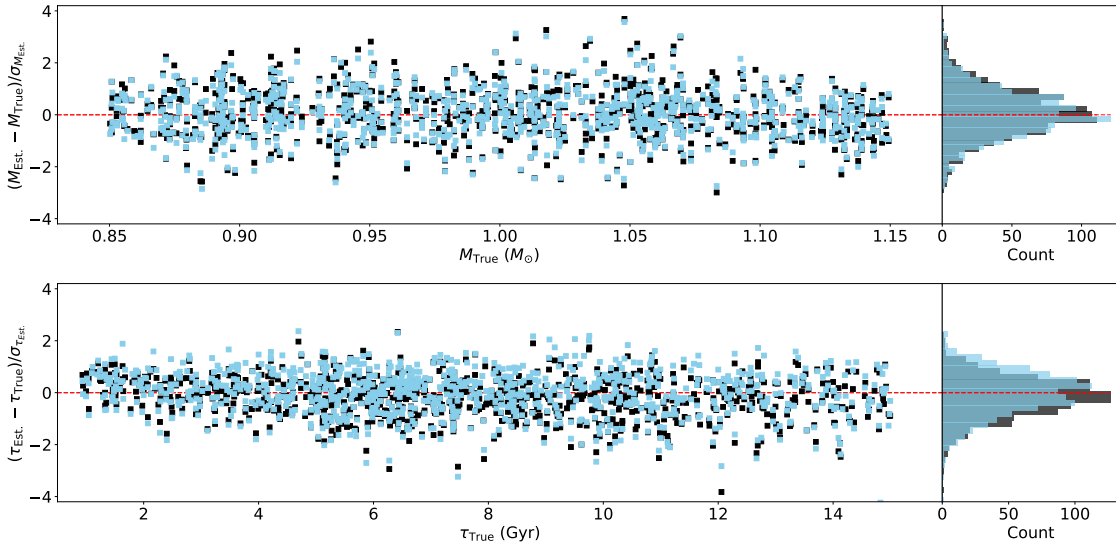


Figure 9. add typical error bars Differences between true and estimated values over estimated uncertainty of 1000 fake stars. Count distributions of offsets are demonstrated on the right side.

A3 Optimiser

We compared two optimisers named SGD and Adam. Here SGD refers to Stochastic Gradient Descent, and Adam is a combination of the advantages of two other extensions of stochastic gradient descent, specifically, Adaptive Gradient Algorithm and Root Mean Square Propagation. The SGD optimiser in the GPyTROCH package involves the formula given by Sutskever et al. (2013). The formula makes it possible to train using stochastic gradient descent with momentum thanks to a well-designed random initialisation and a particular type of slowly increasing schedule for the momentum parameter. The application of momentum in SGD could improve its efficiency and make it less likely to stuck in local minimums. On the other hand, the Adam optimiser includes the 'AMSGrad' variant developed by Reddi et al. (2018) to improve its weakness in the convergence to an optimal solution. With these new developments, the two optimisers give very similar results. We finally choose Adam because it works relatively efficiently and stable. We adaptive learning rate in the training process. Our training starts with a learning rate of 0.01 and decreases by a factor of 2 when the loss value does not reduce in previous 100 iterations.

A4 Early Stopping

We set up an Early Stopping for avoiding overfitting and also determining when to terminate a training progress. When an optimal solution is found, the validating errors stop decreasing and then increase when overfitting occurs. We hence track down the validating error every iteration and terminate training process when the validating error does not decrease in previous 300 iterations.

APPENDIX B: STATE-OF-THE-ART IMPLEMENT FOR LARGE DATASET

In section 4.3, we investigate the strategy for large dataset. We test two State-of-the-art approaches that designed for training big data

whose data size is more than the limit of a GP model. Here we mention some details about the two methods and the results.

We first consider the Stochastic Variational GP (SVGP) approach based on the GPyTorch APPROXIMATEGP module. We train our data based on the SVGP example on https://docs.gpytorch.ai/en/v1.1.1/examples/04_Variational_and_Approximate_GPs/SVGP_Regression_CUDA.html. SVGP is an approximate scheme rely on the use of a series of inducing points which can be selected in the parameter space. It trains using mini batches and hence is able to deal with large data size. The other key point of SVGP is the number of inducing points. Because the kernel is only built on these points, the number determines the complexity of kernel. When the underline function is simple, for instance, a power law, a small number of inducing points is enough. For our application, a large number of inducing points are required. Underline principles and detailed descriptions of this approach can be found in Hensman et al. (2014). In our tests on 3D problem, we find a practical issue with the SVGP approach. When we load in a large training sample which takes a lot GPU memory, the rest memory can capacitate only 10,000 inducing points. This is to say, we use more training data but sacrifice the kernel complexity. The result shows that using SVGP model does not improve the GP predictions compared with normal GP model. For instance, the 68th, 95th, and 99.7th testing errors for T_{eff} are 2.2, 6.8, and 15.1K (EI = 24.1 K) for the SVGP and 2.0, 5.8, and 15.7 K (EI = 23.5K) for the normal GP model. This is because the evolutionary feature are complex across multiple demissions. Reducing the kernel complexity is not ideal. We conclude that the SVGP is suitable for training large data which have relatively simple variations but not a good choice for training the model grid.

We also investigate another approach designed for large dataset named Structured Kernel Interpolation (SKI GP). SKI GP was introduced by Wilson & Nickisch (2015). It produces kernel approximations for fast computations through kernel interpolation and is a great way to scale a GP up to very large datasets (100,000+ data points). We follow the example on https://docs.gpytorch.ai/en/stable/examples/02_Scalable_Exact_GPs/KISSGP_Regression.html to de-

velop our script. We run a few tests to train a 3D SKI GP model with 100,000 training data. Compare with the Normal GP and SVGP, its testing errors for T_{eff} are slightly improved to 2.0, 6.1, and 14.8K (EI = 22.9K). However, the further test on the 5-demission data is not ideal: a SKI GP model using 100,000 training data performs much worse than a normal model with only 20,000 training data. The poor behaviour consists with what has been discussed by Wilson & Nickisch (2015): the SKI GP poorly scale to data with high dimensions, since the cost of creating the grid grows exponentially in the amount of data. We attempt to make some additional approximations with the GPyTorch ADDITIVESTRUCTUREKERNEL module. It makes the base kernel to act as one-dimension kernels on each data dimension and the final kernel matrix will be a sum of these 1D kernel matrices. However, the testing errors are not significantly improved.

REFERENCES

- Asplund M., Grevesse N., Sauval A. J., Scott P., 2009, *Annual Review of Astronomy and Astrophysics*, **47**, 481
- Bain A., 1873, Mind and body: The theories of their relation. Vol. 4, D. Appleton
- Bellinger E. P., Angelou G. C., Hekker S., Basu S., Ball W. H., Guggenberger E., 2016, *ApJ*, **830**, 31
- Bishop C. M., 1994
- Choi J., Dotter A., Conroy C., Cantiello M., Paxton B., Johnson B. D., 2016, *ApJ*, **823**, 102
- Dotter A., 2016, *ApJS*, **222**, 8
- Ferguson J. W., Alexander D. R., Allard F., Barman T., Bodnarik J. G., Hauschildt P. H., Heffner-Wong A., Tamanai A., 2005, *ApJ*, **623**, 585
- Gardner J. R., Pleiss G., Bindel D., Weinberger K. Q., Wilson A. G., 2018, in Advances in Neural Information Processing Systems.
- Hendriks L., Aerts C., 2019, *PASP*, **131**, 108001
- Hensman J., Matthews A., Ghahramani Z., 2014, arXiv preprint arXiv:1411.2005
- Ho T. K., 1995, in Proceedings of 3rd international conference on document analysis and recognition. pp 278–282
- Hon M., Stello D., Yu J., 2018, *MNRAS*, **476**, 3233
- Hon M., Bellinger E. P., Hekker S., Stello D., Kuslewicz J. S., 2020, *MNRAS*, **499**, 2445
- James W., 1890, The principles of psychology. New York, NY: Holt & Co
- Lytle A. J., et al., 2021, *MNRAS*,
- Mombarg J. S. G., Van Reeth T., Aerts C., 2021, arXiv e-prints, p. arXiv:2103.13394
- Paquette C., Pelletier C., Fontaine G., Michaud G., 1986, *ApJS*, **61**, 177
- Paxton B., Bildsten L., Dotter A., Herwig F., Lesaffre P., Timmes F., 2011, *The Astrophysical Journal Supplement Series*, **192**, 3
- Paxton B., et al., 2013, *The Astrophysical Journal Supplement Series*, **208**, 4
- Paxton B., et al., 2015, *The Astrophysical Journal Supplement Series*, **220**, 15
- Paxton B., et al., 2018, *ApJS*, **234**, 34
- Paxton B., et al., 2019, *ApJS*, **243**, 10
- Reddi S., Kale S., Kumar S., 2018, in International Conference on Learning Representations.
- Rendle B. M., et al., 2019, *MNRAS*, **484**, 771
- Rogers F. J., Nayfonov A., 2002, *ApJ*, **576**, 1064
- Schölkopf B., Smola A., Müller K.-R., 1997, in International conference on artificial neural networks. pp 583–588
- Sutskever I., Martens J., Dahl G., Hinton G., 2013, in International conference on machine learning. pp 1139–1147
- Thoul A. A., Bahcall J. N., Loeb A., 1994, *ApJ*, **421**, 828
- Verma K., Hanasoge S., Bhattacharya J., Antia H. M., Krishnamurthi G., 2016, *MNRAS*, **461**, 4206
- Williams C. K., Rasmussen C. E., 1996
- Wilson A., Nickisch H., 2015, in International Conference on Machine Learning. pp 1775–1784
- Wu Y., et al., 2019, *MNRAS*, **484**, 5315

This paper has been typeset from a TeX/LaTeX file prepared by the author.